Mo–Si Alloys Studied by Atomistic Computer Simulations Using a Novel Machine-Learning Interatomic Potential: Thermodynamics and Interface Phenomena

Olena Lenchuk, Jochen Rohrer, and Karsten Albe*

A machine-learning interatomic potential for Mo–Si alloys based on the atomic cluster expansion formalism is presented, its performance is validated, and it is applied for studying interface phenomena. Structural parameters, elastic constants, and melting temperatures of the crystalline body-centered cubic Mo, diamond Si, and stable Mo–Si alloys (Mo_3Si, Mo_5Si_3, and $MoSi_2$) are calculated and compared to experimental values. Using the trained potential defect, formation energies are calculated and the thermodynamic stability of various Mo_xSi_y alloys is discussed with focus on Mo_3Si. Finally, the intermixing between Mo and Si phases is studied by performing interface simulations of Mo|Si. The crystallization behavior of the Mo_3Si phase provides additional evidence for the off-stoichiometric composition of this intermetallic phase.

1. Introduction

Mo-based alloys are promising candidates for high-temperature applications, for example, in gas turbines, due to their high melting temperature and potential for high-temperature strength.[1–4] They allow to increase the operating temperature in the combustion chambers of gas turbine engines to the temperature range 1200–1600 °C, significantly decreasing its efficiency losses.[5,6] The challenge for Mo-based alloy design is the constraints in terms of melting point, oxidation resistance, and structural functionality. The current understanding is that these requirements can only be fulfilled by multicomponent alloys with multiphase microstructures,[7] where the binary molybdenum silicide phases such as Mo_3Si, Mo_5Si_3, and $MoSi_2$ possess excellent high-temperature oxidation resistance and strength but display brittle behavior at room temperature, while the body-centered cubic

(bcc)-type α-Mo solid solution phase provides some ductility but exhibits very low oxidation resistance.[8–11]

The structural and thermodynamic properties of the constituting phases of multiphase microstructures have been studied in much detail over the last decades. Mo_3Si and Mo_5Si_3 were first structurally characterized by Christensen.[12] Mo_3Si crystallizes in the cubic A15 structure, where the Si atoms occupy the bcc positions in the unit cell and the Mo atoms form three orthogonal chains along the <100> directions on the cube faces.[13] The Mo_5Si_3 phase has a complex body-centered tetragonal structure. The crystal structure is characterized by two atomic chains of Mo–Mo and Si–Si atoms, extending along the c-axis with the bond length of 2.45 Å, which are believed to play a significant role in determining thermal and elastic properties of Mo_5Si_3.[14,15] $MoSi_2$ crystallizes in the body-centered tetragonal $C11_b$ crystal structure with two formula units in the unit cell.[16] The atomic structure of the Mo–Si phases is shown in Figure S1, Supporting Information. Later it was shown by Rosales and Schneibel[17] that the A15 Mo_3Si phase is slightly off-stoichiometric, but remains single phase in a small composition range. A crystal viscoplasticity model describing the ductile behavior of α-Mo, including the influence of varying amounts of silicon (Si) in solid solution, was proposed by Brindley and Neu,[10] while the apparently high solubility of Si in α-Mo was studied by means of total energy calculations within density-functional theory (DFT).[18,19] The segregation behavior of Si in a tilt grain boundary of α-Mo was also subject of a computational study.[20] Recently, phase field simulations have been conducted to obtain an understanding of the formation mechanism of the script lamellar pattern of $MoSi_2$/Mo_5Si_3 eutectic composite.[21,22]

Useful insights into structure–property relationships of the constituting phases and the role of interfaces on the overall performance of the multiphase material can also be provided by atomistic simulations. Molecular dynamics (MD) simulations are well established for studying structure and dynamics of materials at finite temperature.[23] The accuracy of atomistic simulations, however, strongly depends on the quality of the interatomic potential describing the interactions between atoms. For the Mo–Si system, a modified embedded atom method (MEAM) potential was proposed by Baskes in 1999.[24] The reported elastic constants, formation enthalpies for the stable Mo–Si compounds (Mo_3Si, Mo_5Si_3, and $MoSi_2$), and the vacancy formation

O. Lenchuk, J. Rohrer, K. Albe
Institute of Materials Science
Technical University Darmstadt
Otto-Berndt-Strasse 3, 64287 Darmstadt, Germany
E-mail: lenchuk@mm.tu-darmstadt.de

The ORCID identification number(s) for the author(s) of this article can be found under https://doi.org/10.1002/adem.202302043.

enthalpies, however, significantly deviate from the experimental values. Therefore, an accurate binary Mo–Si interatomic potential being able to reproduce thermomechanical properties of Mo–So alloys still remains an issue.

Recently, a new potential class based on machine-learning (ML) methods has emerged. The basic idea is ML of the quantitative relationship between local environment descriptors and the potential energy surface of a system of atoms. By using different local environment descriptors, for example, atom-centered symmetry functions, smooth overlap of atomic positions, the spectral neighbor analysis potential (SNAP) bispectrum components, or moment tensors (MT), ML interatomic potentials (MLIPs) interpolate between a known set of training data (energies, forces) generated by DFT.[25–28] It has been shown that MLIPs can be trained which allow to describe a wide range of thermomechanical materials properties.[28–31] For elemental Si and Mo, various MLIPs have been benchmarked by Zuo et al.[29] For silicon, a Gaussian approximation potential (GAP) was also proposed by Bartók et al.[32] which describes point, line and plane defects in silicon. In the study, however, the atomic cluster expansion (ACE) potential approach is employed, which requires significantly less computational resources for highly accurate large-scale atomistic simulations.[33] For example, one single-point DFT calculation using vdW-DF-CX functional requires the central processing unit (CPU) time of around 1–10 min for small-size system (up to ten atoms in the cell), performed on one node with 104 cores per node. Under equal conditions, the MD simulation using ACE potential requires up to 10 s for the calculation. Moreover, the computational cost for the single-point calculation using Mo–Si ACE and the classical MEAM potentials are approximately the same for different system sizes. The noticeable difference in CPU time is observed for supercells containing few millions of atoms. In this case, the MEAM potential requires 1–1.5 min per calculation, whereas the Mo–Si ACE potential in average needs around 3 min.

In the following, we present an interatomic ACE potential for the Mo–Si system and validate its performance. We compute structural parameters, elastic properties, and melting temperatures of the crystalline bcc Mo, diamond Si, and three stable Mo–Si compounds (Mo_3Si, Mo_5Si_3, and $MoSi_2$) and compare calculated properties to experimental values. We also evaluate the silicon solubility in molybdenum and formation enthalpies of Mo and Si vacancies. The thermodynamic stability of intermetallic phases is validated by means of the enthalpy of Mo_xSi_y formation. Eventually, we study intermixing between Mo and Si phases by performing interface simulations of Mo|Si. The crystallization of Mo_3Si phase provides evidences for the off-stoichiometric composition of this intermetallic phase.

2. Results and Discussion

2.1. Training and Validation of the Mo–Si ACE Potential

The starting point for a ML potential is the training database, which in the present case consists of 22 543 atomic model structures (1928 pure Mo, 19 113 Mo–Si models, and 1502 pure Si) and contains 3 097 821 force vectors (5784 pure Mo, 57 339 Mo–Si models, and 4506 pure Si). The sizes of the atomistic models vary from 2 to 300 atoms. For the initial training set, pristine bulk structures were randomly deformed (iso, aniso, and trigonally) with strain levels $|\varepsilon| < 0.05$ and atoms randomly displaced with an standard deviation of 0.05. Based on this database, a first version of the MLIP was trained. Thereafter, crystalline bulk structures (also those containing point defects) were subjected to cook and quench simulations (from well above the melting point) and new test structures were identified using active learning. By successively adding these structures to the training database, the MLIP was improved. The database also includes the molten atomistic structures of Mo, Si, and three Mo–Si compounds, as well as nonground-state structures for all five systems. The total energy in the dataset is corrected by the free atom energies obtained by performing DFT calculations of Mo (Si) atom in a box.[34] In this case, the corrected energy corresponds to the cohesive energy of a system. Further details are given in Section 4. **Figure 1**a shows the distribution of training data projected on energy–volume space for Mo (red dots), Si (blue dots), and Mo–Si intermetallic compounds (yellow dots). The diversity of the training data emerged in this way is reflected by the wide range of energies and volumes and implies good transferability.

The overall accuracy of the ACE potential relative to the DFT reference data is shown in Figure 1b for the energy data. The energy error is shown in Figure 1c. The root-mean-square error (RMSE) is 11 meV atom^{-1} for energies with respect to the complete training database. Restricting the analysis to Mo-only, Si-only, and Mo–Si systems, we find the RMSEs for energies are equal to 17 meV atom^{-1}, 8 meV atom^{-1}, and 10 meV atom^{-1} for the training database, respectively. The RMSEs for forces are equal to 332 meV Å^{-1}, 134 meV Å^{-1} and 247 meV Å^{-1} for the training dataset for Mo-only, Si-only and Mo–Si systems, respectively. The RMSE of the binary Mo–Si ML interatomic potential is higher compared to those reported in the literature for single-element ML interatomic potentials. Zuo et al.[29] report RMSEs in energies from 3.01 meV atom^{-1} (GAP) to 8.45 meV atom^{-1} (SNAP) for Mo and from 3.24 meV atom^{-1} (MT potential) to 10.84 meV atom^{-1} (neural network potential) for Si. The RMSEs in forces, reported by Zuo, vary in a range 0.14–0.37 eV Å^{-1} for Mo and 0.07–0.31 eV Å^{-1} for Si for the training database. The significance of RMSEs is, however, often overestimated because a low RMSE does not guarantee that relevant properties such as lattice parameters, elastic constants, and thermodynamic properties are well reproduced. In **Figure 2–4** and **Table 1–3**, we summarize such physical properties obtained with our MLIP and compare them to experiment, the DFT reference, and the MEAM Mo–Si potential developed by Baskes.[24]

Figure 2 shows the relative deviation, $\Delta V_0 = 100(V^{exp} - V^{ACE})/V^{exp}$, of the computed cell volume (top) and errors of bulk moduli ΔB_0 (bottom) for crystalline Mo, Si, and three stable Mo–Si intermetallic phases. The orange columns show the performance of our ACE Mo–Si potential relative to the experimental values. The values of ΔV_0 and ΔB_0, computed with the van der Waals functional vdW-DF-CX and MEAM Mo–Si potential of Baskes,[24] are also shown for comparison (gray and brown columns, respectively). Experimental data are obtained under ambient conditions (see refs. [35–37]). The results show that the ACE Mo–Si potential accurately reproduces both cell volume and the bulk modulus for all five investigated systems. The largest deviation in equilibrium
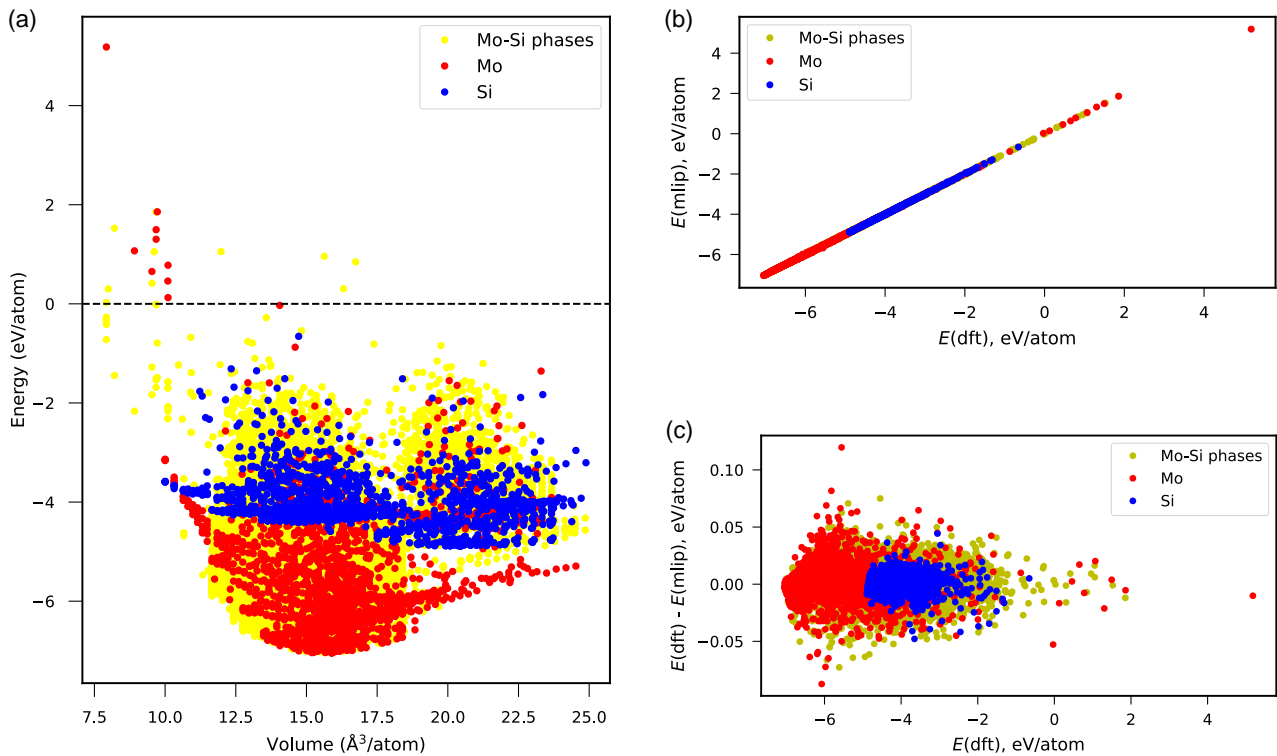
Figure 1. a) The energy–volume relation, b) energy scatter plot, and c) energy error per atom with respect to the DFT energies, computed for the training database. Color coding: molybdenum (red dots), silicon (blue dots), and Mo–Si compounds (yellow dots).
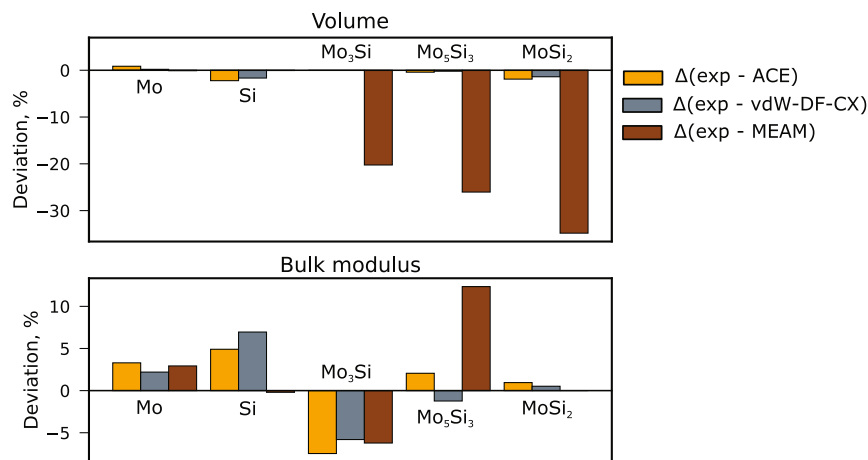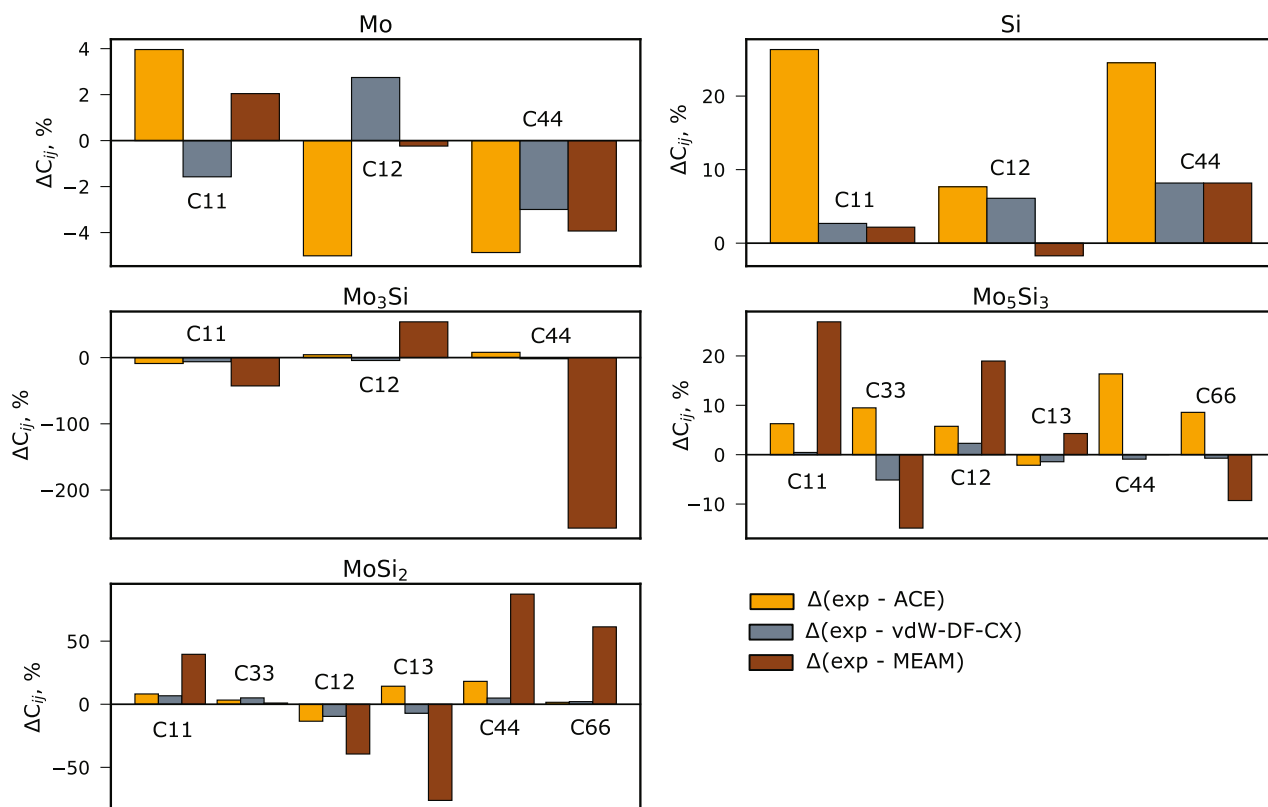

Figure 2. The deviation of the cell volume V and bulk moduli B_0, computed using ACE Mo–Si potential (orange color) and vdW-DF-CX functional (gray color) relative to the experimental values ($\Delta V_0 = 100(V^{exp} - V^{ACE})/V^{exp}$). Data computed using the MEAM Mo–Si potential developed by Baskes[24] are also given for comparison (brown color). The experimental data are provided in refs. [35–37].

volume, ΔV, is observed for silicon and equals to around 2%. In case of bulk modulus, the largest deviation of -7.5% is observed for Mo_3Si. Comparing the performance of ACE and MEAM Mo–Si potentials, the description of the intermetallic phases is being considerably improved if the ACE formalism is applied.

Figure 3 shows the relative deviation of the elastic constants, ΔC_{ij}, computed with respect to experimental data.[35-39] We compare results obtained with the ACE Mo–Si potential (orange

columns), vdW-DF-CX functional (gray columns), and the MEAM Mo–Si potential developed by Baskes[24] (brown columns). The values for ΔC_{ij} are shown for crystalline Mo, Si, and three Mo–Si bulk compounds (see Section 4 for details). The absolute values of the corresponding elastic constants are summarized in Table S5, Supporting Information. The relative deviation is the smallest for Mo and for Mo_3Si phases for all computed elastic constants. The largest relative deviation ΔC_{ij} of

ADVANCED
SCIENCE NEWS

www.advancedsciencenews.com

ADVANCED
ENGINEERING
MATERIALS

www.aem-journal.com

Figure 3. The relative deviation of the elastic constants ΔC_{ij}, computed using our ACE Mo–Si potential, relative to the experimentally measured values. The MEAM Mo–Si potential of Baskes[24] and van der Waals functional (vdW-DF-CX) are also shown for comparison. The experimental data are provided in refs. [35–39].
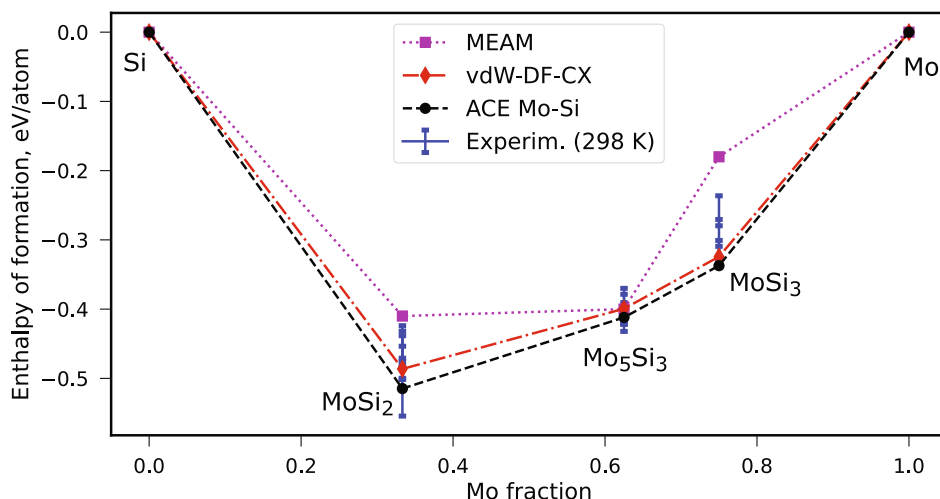
Figure 4. The formation enthalpy of molybdenum silicides (Mo_3Si, Mo_5Si_3, and $MoSi_2$) obtained by the ACE Mo–Si interatomic potential. The computed data are compared to DFT values using the vdW-DF-CX functional. The experimentally defined standard enthalpies of formation are defined at 298 K.[65–73]

around 25–26% is observed for silicon. The elastic constants C_{44} and C_{66} correspond to shear on (100) and (001) planes, respectively. For both tetragonal compounds, Mo_5Si_3 and $MoSi_2$, C_{44} is smaller than C_{66}, reflecting that atoms in the basal plane in both compounds are stronger bonded compared to the atoms along [001] directions. In Mo_5Si_3, the Mo–Mo and Si–Si chains are present along the [001] direction and the Mo–Si–Si chains in $MoSi_2$. The larger C_{66} compared to C_{44} also indicates the thermal

Table 1. The calculated melting temperature of Mo, Si, and Mo–Si intermetallic compounds, obtained using our ACE Mo–Si potential.

Material	Mo [K]	Mo$_3$Si [K]	Mo$_5$Si$_3$ [K]	MoSi$_2$ [K]	Si [K]
Moving boundary	2913 ± 13	2363 ± 13	2363 ± 13	2288 ± 13	1300
Calphy	2907	2360	2371	2288	1299
Experiment[4,6,48]	2896	2298	2453	2303	1687

Table 2. The calculated heat of solution (H_s) of substitutional silicon atom in crystalline molybdenum. The relaxation volume V_{rel} of a defect is obtained using Equation (8) relative to the atomic volume of Mo atom (Ω).

	ACE	vdW-DF-CX	PBE (our study)[18]
H_s [eV]	0.97 eV	0.91	0.87
V_{rel} [Ω]	−0.17	−0.17	−0.10

expansion anisotropy of both compounds.[4,15,40] Overall, the ACE Mo–Si potential improved on the description of elastic constants for Mo$_x$Si$_y$ intermetallic phases significantly as compared to the existing MEAM Mo–Si potential.

In addition to the elastic properties, an accurate interatomic potential should also correctly describe the thermodynamic stability of competing phases. Therefore, we validate the ACE Mo–Si potential further and compute the enthalpies of formation (H_f) for molybdenum silicides. The computed H_f are calculated using Equation (3) and are shown in Figure 4. The formation enthalpies show the correct sequence for intermetallic compounds, namely, $H_f(\text{MoSi}_2) < H_f(\text{Mo}_5\text{Si}_3) < H_f(\text{Mo}_3\text{Si})$ and agree with experimental data within the uncertainty. The formation enthalpies computed for all structures, provided in the training and testing datasets, are shown in Figure S7, Supporting Information. The MEAM Mo–Si potential developed by Baskes (magenta squares)[24] also agrees well with the experimental data for Mo$_5$Si$_3$, but erroneously describes the Mo$_3$Si phase as unstable.

Finally, we complete the verification of the ACE Mo–Si potential by computing the melting temperatures for crystalline Mo, Si, and the intermetallic compounds, Mo$_3$Si, Mo$_5$Si$_3$, and MoSi$_2$. Table 1 lists the computed melting points, T_m, obtained using the moving-boundary method[41] and by comparison of free energies calculated by thermodynamic coupling-constant integration as implemented in the calphy package[42] (see Section 4 for details). For the latter method, there is excellent

agreement with the moving-boundary technique. For pure Mo and MoSi$_2$ there is very good agreement between calculated and measured melting points, for Mo$_3$Si and Mo$_5$Si$_3$ there is reasonable agreement, and only for Si we see a strong underestimation of our potential. This underestimation is most likely due to the small amount of molten Si in the training database. However, here the focus is mainly on the intermetallics and not on the boundary phases.

In the following, we apply the ACE potential to study point defects and the stability range of the Mo$_3$Si phase and mixing processes of Mo and Si.

2.2. Point Defects

The solubility of silicon in molybdenum below 1200 °C is $\approx$1 at.% or lower.[43] The high-temperature measurements, however, report a much larger solubility of around 4 at.% Si in Mo near the peritectic temperature ($T = 2298$ K).[44–47] The theoretical solubility at the peritectic temperature of 2298 K that corresponds to the reaction "liquid + Mo$_{ss}$ → Mo$_3$Si"[6] is less than 1 at.% (see Table 2), if only the formation enthalpy is considered. Sun et al.[19] however, have shown that the high solubility of Si at 2000 K can be explained in terms of equilibrium thermodynamics, when the vibrational entropy, and thus the free energy of formation (not only the enthalpy) is used. Moreover, the presence of grain boundaries also affects the solid solubility limit. Our study of Si segregation at Mo grain boundaries (GBs) and surfaces using the Perdew-Burke-Ernzerhof (PBE) functional[82,83] has shown that the silicon formation enthalpy is considerably reduced at Mo GBs and Mo surfaces compared to the bulk.[20] Thus, for benchmarking the ACE potential we are only comparing the calculated heat of solution H_s and relaxation volume of silicon in crystalline molybdenum. Table 2 lists the calculated values for substitutional Si in α-Mo in the dilute limit (see Section 4 for computational details).

The heat of solution obtained using the ACE Mo–Si potential corresponds to 0.97 eV, whereas the vdW-DF-CX functional gives 0.91 eV. The results show that ACE Mo–Si potential overestimated the obtained heat of solution (0.97 eV) compared to the H_s computed using vdW-DF-CX functional (0.91 eV), showing, however, the same order of magnitude. The positive sign of the heat of solution indicates that the dissolution of Si from Mo$_3$Si into Mo as a solid solution is an endothermic process.[18] The relaxation volume ΔV_{rel} is computed using Equation (8) relative to the atomic volume of Mo atom, Ω. The negative value of the ΔV_{rel} indicates that the host lattice is contracted due to the

Table 3. Formation enthalpy H_f of Mo and Si vacancy in crystalline α-Mo, Si, and Mo$_x$Si$_y$, obtained using Equation (4) and (5). The H_f is given for upper and lower thermodynamic bounds for Mo and Si chemical potentials, defined by Equation (6) and (7), respectively. All numbers are given in eV. The relaxation volume of the vacancy is calculated according to Equation (8) relative to the atomic volume of the corresponding element in the host lattice, Ω.

	Mo vacancy			Si vacancy			
System	$\mu_{Mo}^{Mo-rich}$	$\mu_{Mo}^{Mo-poor}$	V_{rel} [Ω]	$\mu_{Si}^{Si-rich}$	$\mu_{Si}^{Si-poor}$	V_{rel} [Ω]	Experiment [eV]
α-Mo	3.50	–	−0.34	–	–	–	3.0,[74] 3.2,[75] 3.6,[74] 3.67[76]
Si	–	–	–	3.10	–	−1.5	2.4,[77] 2.5,[78] 3.6,[79] 4.0[80]
Mo$_3$Si	3.22	2.77	−0.46	4.37	3.023	−0.27	–
MoSi$_2$	3.99	2.45	−0.15	2.81	2.04	−0.21	1.6,[49] 1.7[81]

presence of a defect. Both values are in good agreement to the DFT data, which have not been part of the training database.

Also, vacancy formation and transport is a key property, if, for example, creep simulations of the Mo–Si multiphase compounds are intended. Thus, we calculate formation enthalpies of vacancies in crystalline Mo, Si, and in Mo–Si compounds. The defect formation enthalpy depends on the chemical potentials of the elements, which are exchanged with the reservoir in order to create the point defect (see Section 4). The range of molybdenum (silicon) chemical potential μ_{Mo} (μ_{Si}) in Mo–Si system can be established using thermodynamic bounds for the chemical potentials for Mo and Si atoms, respectively. Table 3 summarizes the obtained results for crystalline α-Mo, Si, and three stable Mo–Si intermetallic compounds. The vacancy formation enthalpy of Mo in crystalline molybdenum and of Si in bulk silicon lies within the range for experimentally measured values. The vacancy relaxation volume V_{rel} represents the change in pressure due to the presence of the vacancy in the supercell. The V_{rel} is given relative to the atomic volume of Mo (Si) in a defect-free host lattice, Ω. Negative values of V_{rel} correspond to a contraction of the host lattice. The relaxation volume for Si vacancy in diamond structure is the largest among the investigated structures.

For Mo_xSi_y compounds, Mo- and Si-vacancy formation enthalpies strongly depend on the chosen chemical potential for Mo (Si) atom. The H_f lies within the range defined by using the above-described thermodynamic bounds for μ_{Mo} and μ_{Si}. The experimental and theoretical studies on point defects in $MoSi_2$ agree that the thermal vacancies up to the highest temperatures are predominantly formed on the Si sublattice.[48–50] Moreover, the difference between the Mo and Si diffusivities is about six orders of magnitude near 1500 K.[49] Huang[50] and Li[48] report the formation enthalpies of Mo vacancy in $MoSi_2$ using PBE functional. The authors report the computed H_f of 3.23 eV and 3.54 eV for Mo vacancy, whereas for Si vacancy the H_f equals to 2.10 eV and 2.31 eV, respectively. Our results given for Mo-rich conditions agree with these theoretical investigations. In contrast, the vacancy formation enthalpies, computed in the study of Baskes using MEAM Mo–Si potential,[24] are considerably higher than available data. Thus, H_f corresponds to 12.0 eV for Mo vacancy and 5.8 eV for Si vacancy in $MoSi_2$. For Mo_3Si, the H_f equals to 9.4 eV for Mo vacancy and 7.1 eV for Si vacancy.

2.3. Mo$_3$Si Composition Range

One of the open questions concerning the Mo_3Si compound is the width of its phase field. In the Mo–Si phase diagram studied by Okamoto,[45] Mo_3Si is depicted as a line compound. The study of Ha et al.[51] found that the compositional limit of Si varies by ±1 at.%. The composition of the Mo–Mo_3Si alloys was examined using various experimental methods.[52] The authors state that the average content of Si was lower than 25 at.%. Thus, Si concentration was around 23.6 at.% in the sintered sample and 22.3–22.6 at.% in the melt-quenched samples. Moreover, the authors could not achieve a stoichiometric composition of 25 at.% Si even after high-temperature annealing of the melted samples. Rosales and Schneibel[17] also confirm that the Mo_3Si silicide is not precisely stoichiometric, nor is it a true line compound. Its single-phase composition is near Mo–24 at.% Si.

The concentration of Si in Mo_3Si phase can be varied by introducing point defects in the cell. For this purpose, we constructed supercells containing Mo and Si vacancies, as well as antisites defects (Mo occupying Si site and Si occupying Mo site) in different concentrations. The calculations are performed using a supercell containing 162 Mo and 54 Si atoms under NVE conditions (constant particle number N, constant volume V and a conserved internal energy E). We compute the formation enthalpy of Mo_3Si compound containing point defects, ΔH_f (with defect), using Equation (3). Varying the concentration of defects in the cell, the contribution of the configurational entropy S_{conf} can further stabilize the system, especially taking into account the experimental temperature range for Mo_3Si phase formation. The configurational entropy is computed according to[53]

$$\Delta S_{conf} = -R(x_{Mo}\ln x_{Mo} + x_{Si}\ln x_{Si}) \tag{1}$$

where R is the universal gas constant. The mole fraction of Mo atoms and of Si atoms in $Mo_{3+x}Si_{1-x}$ compound is given by x_{Mo} and x_{Si}, respectively. Finally, we subtract the $T\Delta S_{conf}$ term from the formation enthalpy of $Mo_{3+x}Si_{1-x}$.

Figure 5 shows the computed Gibbs free energy of formation, ΔH_f (with defect) $- T\Delta S_{conf}$, of Mo_3Si containing different points defects for $T = 300$ K. Our results indicate that the variation in Mo_3Si composition can be first of all achieved by introducing antisite defects, when Mo occupies the sites of Si atoms (cyan rhombs). At room temperature, the $T\Delta S_{conf}$ term equals to 14 meV atom^{-1} for 78 at.% Mo in Mo_3Si and stabilizes the phase with given composition compared to the stoichiometric Mo_3Si with 75 at.% Mo (black dashed line). When the temperature is further increased, structures containing other point defects also become stable. For example, at 800 K the $T\Delta S_{conf}$ term equals already 37 meV atom^{-1}. At this temperature, Mo_3Si containing 1 at.% of Si vacancies and Si occupying Mo site are also stable. However, the most significant impact on the composition is provided by Mo occupying Si sites. Our results, obtained using the ACE Mo–Si potential, are thus consistent with experimental studies regarding the not precisely stoichiometric composition of Mo_3Si phase.

2.4. Mo and Si Phases Interactions

2.4.1. Intermixing of Mo and Si Phases

Mo–Si alloys are relevant for high-temperature applications. Therefore, an interatomic Mo–Si potential should be able to describe the thermodynamic properties and kinetics of the alloy at elevated temperatures. In the following section, we investigate the driving force for intermixing between Mo and Si phases. For this purpose, we construct Mo(001)/Si(001) interfaces with different ratios between Mo:Si atoms. The atomistic model for simulations is shown in **Figure 6**a. The supercells contain 14 112 Mo and 4608 Si atoms (Mo:Si ration of around 3:1), 5292 Mo and 11 520 Si atoms (Mo:Si ration of around 1:2), as well as 588 Mo and 512 Si atoms (Mo:Si ration of around 1:1). The supercell dimensions in x- and y- directions are fixed to those of Mo at 2300 K. Each supercell includes also a 20 Å vacuum layer. The simulations are performed under NVT conditions and the system is equilibrated at 2300 K for 20 ns.
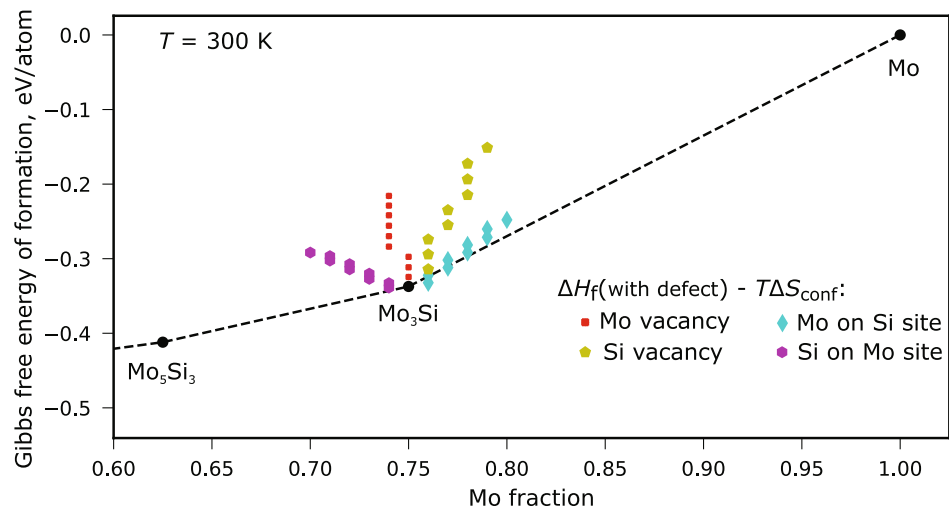
Figure 5. The Gibbs free energy of formation, ΔH_f (with defect) $- T\Delta S_{conf}$, computed for Mo_3Si compound containing different point defects. Color coding: Mo vacancy (red dots), Si vacancy (yellow pentagons), Mo occupying Si atom site (cyan rhombs), and Si occupying Mo atom site (purple circle).
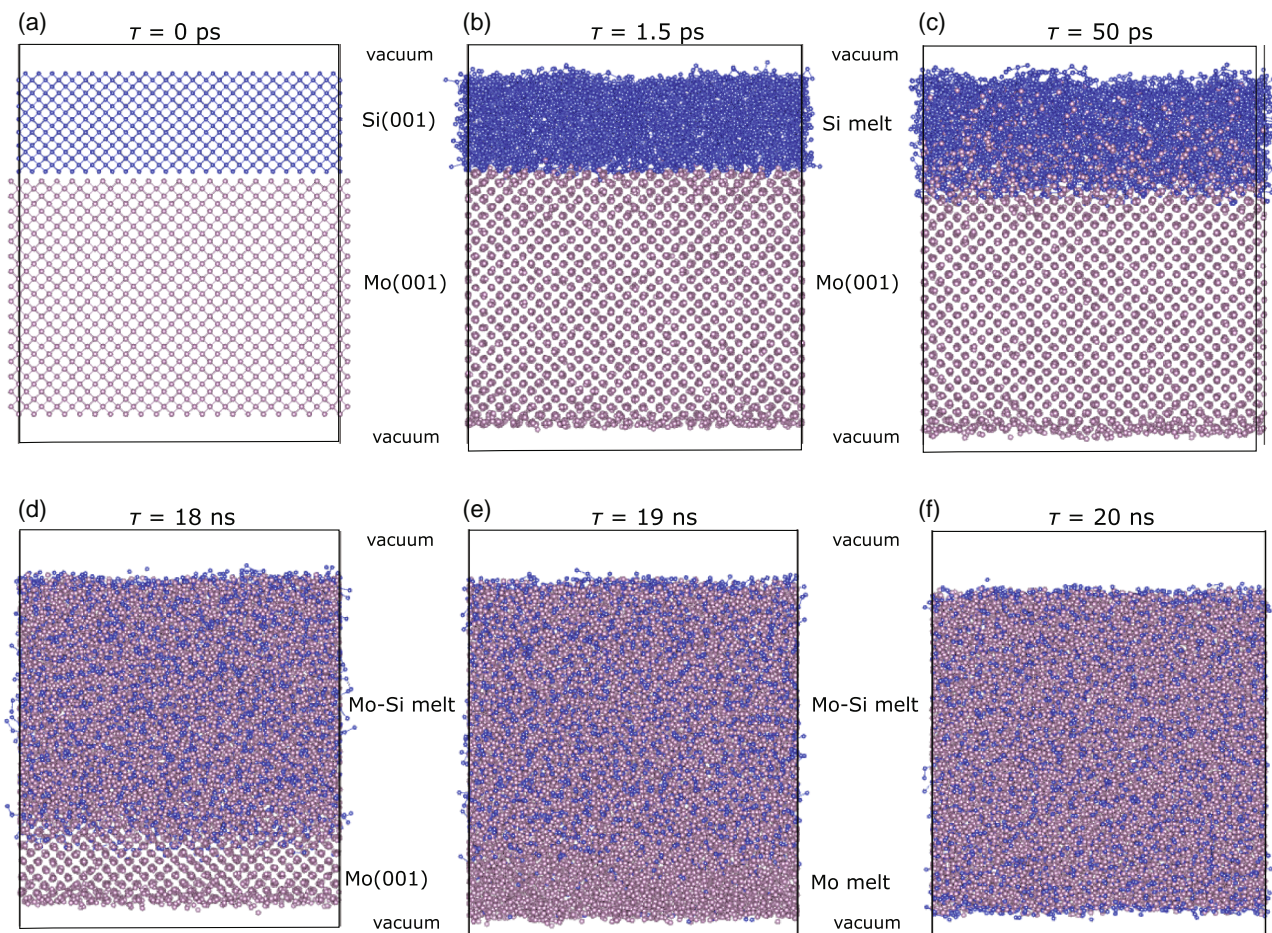
Figure 6. a) Atomistic model of Mo(001)/Si(001) interface. The ratio of Mo:Si atoms corresponds to approximately 3:1. The Mo(001)/Si(001) is equilibrated at 2300 K. Snapshots of the Mo–Si mixing process are given at time step b) 1.5 ps, c) 50 ps, d) 18 ns, e) 19 ns, and f) 20 ns.

The simulations using the ACE Mo–Si potential show a high driving force for intermixing between Mo and Si phases. Snapshots for different timesteps are shown in Figure 6b–f. The results show that Si melts immediately as expected, whereas the molybdenum phase remains crystalline. Both phases are equilibrated at 2300 K, which is well above the melting temperature of silicon (see Table 1). Further on, Mo atoms at the Mo(001)/Si melt interface start to diffuse into Si melt, creating Mo–Si mixture. Silicon atoms also diffuse into Mo bulk but in much smaller amount and at very small distances. The Mo–Si melt grows involving more and more Mo atoms from the crystalline Mo and the interface between Mo–Si melt and bulk Mo moves toward the Mo(001) surface (see Figure 6c,d). At around 19 ns, the remaining thin layer of bulk molybdenum of around 10–12 Å also melts (see Figure 6e). Afterward, Si atoms can diffuse through the molybdenum melt to the Mo(001) surface. At timestep of 20 ns, both Mo and Si phases are fully mixed, showing excess of Si atoms at the surfaces. Simulations performed for other Mo:Si atoms ratios follow the same scenario.

Figure 7 shows the radial distribution function (RDF), computed for Mo(001)/Si(001) interface at different intermixing steps (see Figure 6 for details). The RDF is calculated using OVITO software.[54] At timestep zero, the sharp peaks correspond to the average distance of 2.40 Å between Si atoms and 2.76 Å between Mo atoms (see Figure 6a). When Mo and Si

atoms are fully mixed, Mo are dominantly surrounded by another Mo and by Si atoms. The RDF is very similar to that obtained for molten Mo_3Si (see Figure 6d). The analysis of the RDF suggests that both Mo and Si phases are fully mixed, resulting in a Mo–Si mixture with distribution of Mo and Si atoms similar to molten Mo_3Si phase. The bond analysis shows an average bond lengths of 2.60 Å for Mo–Si and 2.81 Å for Mo–Mo and a wide range of atoms coordination, from 4 to 10. In the pristine Mo_3Si crystal, the atoms are 12- and 14-fault coordinated, with bond length of 2.73 Å for Mo–Si (four bonds), 2.44 Å (two bonds), and 2.99 Å (eight bonds) for Mo–Mo atoms.
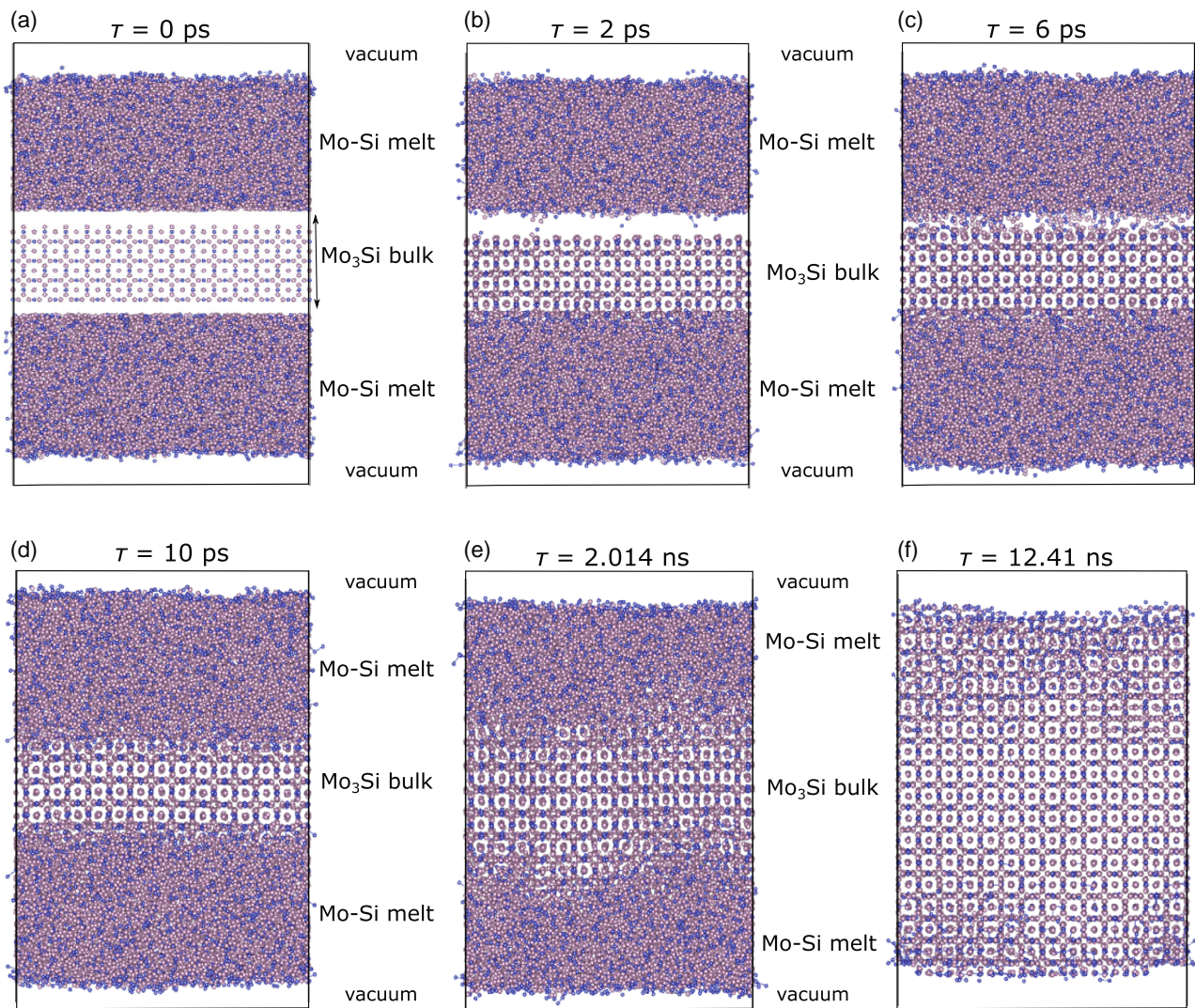
2.4.2. Off-Stoichiometric Mo_3Si Phase Crystallization

In Section 2.3, we have shown that Mo_3Si phase exhibiting the off-stoichiometric composition can be thermodynamically stable if we take into account the configurational entropy of antisite defects (Mo occupying sites of Si atoms). As the next step, we investigate the crystallization of Mo_3Si performing MD simulations. For this purpose, we inserted a thin layer of crystalline Mo_3Si containing four stoichiometric units ($\approx$19.6 Å thick) in the middle of the supercell containing molted and mixed Mo–Si phase with around 3:1 ratio of Mo:Si atoms (14 112 Mo and 4608 Si atoms), obtained after equilibration at 2300 K for 20 ns (shown
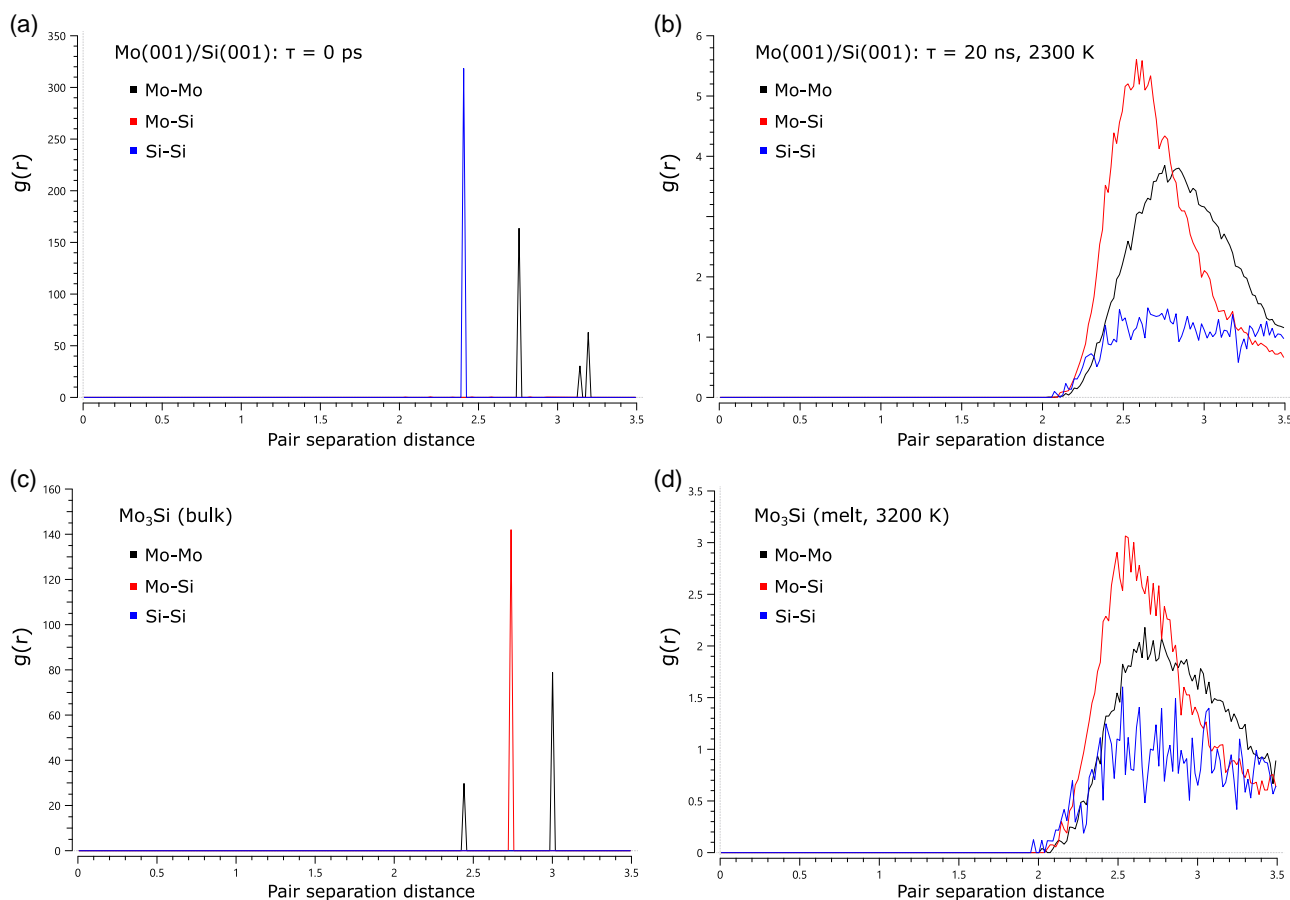
Figure 7. RDF, computed for Mo(001)/Si(001) interface at different intermixing steps: a) 0 ps and b) 20 ns. RDF for c) Mo_3Si bulk and d) Mo_3Si melt, prepared at $T = 3200$ K.

**ADVANCED
SCIENCE NEWS**

www.advancedsciencenews.com

**ADVANCED
ENGINEERING
MATERIALS**

www.aem-journal.com

Figure 8. Snapshots of the Mo₃Si crystallization process. A crystalline layer of stoichiometric Mo₃Si is located inside the molten Mo–Si phase. The Mo:Si atoms ratio in the molten Mo–Si phase is around 3:1 with slight Mo excess (14 112 Mo and 4608 Si atoms). Atomistic structures are shown a) at zero timestep (τ), b) at 2 ps and ≈2300 K, c) at 6 ps and ≈2300 K, d) at 10 ps and ≈2290 K, e) at 2.014 ns and ≈2115 K, and f) 12.41 ns and ≈1355 K.

in Figure 6). The lattice parameters of the supercell in *x*- and *y*-directions have been rescaled to those of bulk Mo₃Si at 0 K, obtained after structure optimization. The system is cooled down from 2300 K to 300 K for 20 ns under NVT conditions.

Figure 8a–f shows the snapshots of the crystallization process. In the beginning, the bulk Mo₃Si phase moved closer to the Mo–Si melt. The crystalline and molten phases are separated by vacuum layer of around 3 Å thickness in order to prevent the atoms to overlap. This distance is within the 5 Å cutoff radius of the ACE Mo–Si potential and the reaction between crystalline Mo₃Si and Mo–Si melt takes place. Afterward, another part of the Mo–Si melt also reacts with the bulk Mo₃Si (see Figure 8c). At time step of around 10 ps, the bulk Mo₃Si starts to grow and at time step of 12.41 ns the crystallization is almost competed; the Mo₃Si phase is extended through the volume reaching both surfaces. Figure 8f shows that the grown crystalline Mo₃Si phase is not precisely stoichiometric and contains antisite point defects

with Mo occupying sites of Si atoms, whereas Si atoms in excess are segregated at both surfaces. The results of the dynamic simulations confirm our findings regarding the thermodynamic stability of Mo₃Si at different composition (see Figure 5). The Mo₃Si compound with excess of Mo atoms can be stabilized by introducing antisite defects.

3. Conclusions

A new ACE MLIP widely applicable to binary for Mo–Si system is developed. It is able to reproduce the lattice parameters, elastic constants, and melting points of crystalline Mo, Si, and three stable Mo–Si intermetallic phases with good accuracy in comparison with experimental data. The ACE Mo–Si potential also predicts the stability of three molybdenum silicide phases, Mo₃Si, Mo₅Si₃, and MoSi₂. The computed enthalpy of formation for

each phase lies within the experimentally defined accuracy limits. The calculated formation enthalpies of different point defects (substitutional Si, Mo, and Si vacancies) using our ACE Mo–Si ML interatomic potential show good agreement to the DFT data (PBE functional), although they have not been part of the training database. Interface simulations of Mo|Si are performed to study the intermixing between Mo and Si phases. Thermodynamic analysis of the Mo_3Si phase shows that the off-stoichiometric composition of Mo_3Si can be achieved by introducing antisite defects (Mo occupying sites of Si atoms) if taking into account the configurational entropy term. Moreover, MD simulations of the Mo_3Si crystallization also provide evidence for the presence of antisite defects and the off-stoichiometry of the grown Mo_3Si.

4. Experimental Section

MD: MD simulations were performed using LAMMPS software.[55] We used a time step of 1 fs, a temperature damping constant of 100 fs, and a pressure damping constant of 1000 fs. Each phase is minimized using conjugate gradient minimization routine to energy (unitless) and force (eV Å^{-1}) stopping tolerances of 10^{-15}. The optimized structures of Mo, Si, and Mo–Si compounds are used further to compute the bulk modulus B_0 and the elastic constants C_{ij}. The bulk modulus is obtained by fitting the energy–volume data of the optimized cell to the third-order Birch–Murnaghan equation of state.[56,57]

Elastic constants characterize the stiffness of a material. Applying small strains to the solid, the elastic constants C_{ij} are computed by fulfilling the relationship between the total energy changes (ΔE) and the strains (ε_{ij}) according to Hooks law[58]

$$\Delta E = \frac{V_0}{2} \sum_{i,j=1}^{6} C_{ij} \varepsilon_i \varepsilon_j \tag{2}$$

where V_0 is the unit cell volume. The strain tensor is provided by LAMMPS/ELASTIC package.

In order to define the vacancy formation enthalpy H_f^{vac} and the heat of solution H_s for substitutional Si atom in Mo bulk, MD simulations in bulk crystal are performed with supercells containing 16 to more than 4000 atoms and held in an NVE ensemble. The computed values of H_f (H_s) given in the results section are provided in the dilute limit and did not change upon further increase of the supercell size.

The melting temperatures of Mo, Si, and Mo–Si intermetallic phases are derived using the moving-boundary method,[41] as well as performing calculations using the calphy package.[42] For the latter case, the melting temperature is computed using a combination of free energy calculation and temperature sweep. The variation of the free energy within the specified temperature range is computed for solid and liquid reference states and the melting point is defined as a point where both phases have the same free energy. Supercells containing over 17 000 atoms are used and temperature sweep calculations are carried out over 300 000 switching steps.

DFT: Total-energy single-point calculations are carried out using the plane-wave projector-augmented wave (PAW[59,60]) code GPAW,[61,62] with the vdW-DF-CX exchange–correlation functional.[63] We use plane-wave cutoff of 900 eV and k-points density of 8 points Å^{-1} for small- and middle-size (containing up to 128 atoms) metallic systems. For Si and large metallic systems, k-points density is reduced to 6 points Å^{-1}.

Training Database: The ACE formalism was chosen for fitting a MLIP for the binary Mo–Si alloy. Our training dataset consists of configurations with crystalline Mo, Si, and three stable intermetallic phases, Mo_3Si, Mo_5Si_3, and $MoSi_2$. It includes the ground-state configurations with lattice parameters close to experimental values and those where the cells are deformed and atoms are rattled. In this case, the small strains ε_{11}, ε_{22}, and ε_{33} from 0% to 5% are applied. In case of isotropic deformation, the strains

$\varepsilon_{11} = \varepsilon_{22} = \varepsilon_{33}$ are equivalent. For anisotropic deformation, the strain value was randomly chosen in a given strain range. The training database also includes crystalline phases with point defects. Among point defects, vacancies, substitutional atoms, and antisite defects in concentration between 0.4% and 6.25% are considered for bulk phases. Furthermore, one of the implementations of Mo–Si potential we are interested in is the description of the Mo–Si phase diagram. Therefore, our training database also includes molten structures of Mo, Si, and Mo–Si compounds. The amorphous structures are obtained by heating up and equilibrating the system with MTP Mo–Si potential, developed earlier. The corresponding supercells include between 216 atoms (for molten Si) and 300 atoms (for molten $MoSi_2$) and are equilibrated at temperatures equal to 4000 K for Mo, 3200 K for Si, and 3750 K for Mo–Si intermetallic compounds for 0.8 ns. In addition to molten structures, the non-ground-state structures of various lattice parameters (bcc or diamond, simple cubic, face-centered cubic, tetragonal centered) for Mo and Si are also considered. For Mo–Si, we include zincblende, skutterudite, and cesium chloride structures into a training database. In total, the training dataset contains 22 543 atomic structures. In order to achieve a better fit, a cutoff of 60.05 eV Å^{-1} for a maximum absolute force and a cutoff of 24.99 Å^3 atom^{-1} for atomic volume are set for all structures in the training dataset. Furthermore, a testing dataset consists of 3380 atomic structures (308 for Mo, 207 for Si, and 2865 for Mo–Si compounds), which have been randomly chosen from the training dataset and additionally rattled (stdev = 0.05). The RMSEs for the testing database are equal to 11 meV atom^{-1} for energy and 257 meV Å^{-1} for forces.

The pacemaker code[33,34] is used for fitting ACE potential for binary Mo–Si system. The total number of basis functions used for fitting is equal to 606 per element. The implementation of higher amount of the basis functions did not improve the accuracy of the potential. The cutoff of 5 Å is set for the neighbor list. The value for the relative weight for energies and forces in the loss function is set to 0.99 and 0.01, respectively. In order to get the balanced distribution of the training energies and forces in the loss function, the value of the loss function is chosen based on the distribution of RMSEs for energies and forces, defined for the training dataset (see Figure S9, Supporting Information). The total energy in both datasets are corrected by the free atom energies obtained by performing DFT calculations of Mo (Si) atom in a box, as recommended in ref. [34]. In this case, the corrected energy corresponds to the cohesive energy of a system. The energy–volume curves for the various non-ground-state structures for crystalline Mo, Si, and three Mo–Si compounds are shown in Figure S2–S6, Supporting Information, and the corresponding lattice parameters, cohesive energies for Mo and Si, and formation energies for Mo–Si phases are summarized in Table S1–S4, Supporting Information.

Energetics: The formation enthalpy H_f of Mo_xSi_y intermetallic compound is obtained according to

$$H_f = (E_{Mo_xSi_y} - x \times \varepsilon_{Mo} - y \times \varepsilon_{Si})/(x + y) \tag{3}$$

Here, $H_{Mo_xSi_y}$ is the total energy of Mo_xSi_y cell. The total energy of the bulk bcc Mo and diamond Si, computed per atom, is defined as ε_{Mo} and ε_{Si}, respectively.

The Mo-vacancy formation enthalpy H_f^{vac} in crystalline Mo or Mo_xSi_y phases is computed using the following equation

$$H_f^{Mo-vac} = E_{Mo_{x-1}Si_y}^{cell\,with\,defect} - E_{Mo_xSi_y}^{defect-free} + \mu_{Mo} \tag{4}$$

and for the Si vacancy

$$H_f^{Si-vac} = E_{Mo_xSi_{y-1}}^{cell\,with\,defect} - E_{Mo_xSi_y}^{defect-free} + \mu_{Si} \tag{5}$$

Here, $E^{cell\,with\,defect}$ and $E^{defect-free}$ are the total energies of the perfect, defect-free Mo_xSi_y supercell and one containing a vacancy, respectively. The size of the unit cell was increased until the vacancy formation enthalpy does not change. The chemical potentials of Mo and Si are represented by μ_{Mo} and μ_{Si}, respectively. For Mo-rich conditions, μ_{Mo} achieves its maximum value and equals to those of bulk bcc Mo

$$\mu_{Mo}^{Mo-rich} = \varepsilon_{Mo} \tag{6}$$

For Mo-poor conditions, the μ_{Si} reaches its maximum value and equals to those of crystalline Si in diamond lattice and the Mo chemical potential can be computed as

$$\mu_{Mo}^{Mo-poor} = \frac{1}{x}(\varepsilon(Mo_xSi_y) - y \times \varepsilon_{Si}) \tag{7}$$

The relaxation volume is computed according to[64]

$$V_{rel} = 1/3 \times Tr(P_{\alpha\beta}) \times V_0/B_0 \tag{8}$$

$1/3Tr(P_{\alpha\beta})$ is the hydrostatic part of the stress tensor, which corresponds to the pressure change due to the presence of the point defect in the material with the equilibrium volume V_0 and the bulk modulus B_0.

For Si, the heat of solution is defined as follows

$$H_{s,Si} = E_{Mo_xSi_y}^{subst-Si} - y \times \varepsilon_{Mo_3Si} - (x - 3y) \times \varepsilon_{Mo} \tag{9}$$

where $E_{Mo_xSi_y}^{subst-Si}$ is the total energy of the Mo supercell containing a substitutional Si atom. Upon increasing Si content in the bulk molybdenum, it will be in equilibrium with the Mo_3Si phase.[45] Therefore, we choose Mo_3Si as a reservoir for Si.

Supporting Information

Supporting Information is available from the Wiley Online Library or from the author.

Conflict of Interest

The authors declare no conflict of interest.

Data Availability Statement

The data that support the findings of this study are openly available in ZENODO at https://zenodo.org/records/10245468, reference number 10245468.

Keywords

machine-learning interatomic potentials, molecular dynamics, Mo–Si alloys, refractory alloys

[1] J. Perepezko, *Science* **2009**, *326*, 1068.

[2] J. Schneibel, C. Liu, D. Easton, C. Carmichael, *Mater. Sci. Eng., A* **1999**, *261*, 78.

[3] D. Dimiduk, J. Perepezko, *MRS Bull.* **2003**, *28*, 639.

[4] L. Jiang, B. Zheng, C. Wu, P. Li, T. Xue, J. Wu, F. Han, Y. Chen, *Processes* **2022**, *10*, 9.

[5] M. Zhao, W. Ye, M. Zhu, Y. Gui, W. Guo, S. Wu, Y. Yan, *Materials* **2023**, *16*, 3.

[6] O. Kauss, S. Obert, I. Bogomol, T. Wablat, N. Siemensmeyer, K. Naumenko, M. Krüger, *Metals* **2021**, *11*, 564.

[7] J. Perepezko, M. Krüger, M. Heilmaier, *Mater. Perform. Charact.* **2021**, *10*, SI 122.

[8] M. Akinc, M. Meyer, M. Kramer, A. Thom, J. Hübsch, B. Cook, *Mater. Sci. Eng., A* **1999**, *261*, 16.

[9] M. Krüger, S. Franz, H. Saage, M. Heilmaier, J. Schneibel, P. Jehanno, M. Böning, H. Kestler, *Intermetallics* **2008**, *16*, 933.

[10] K. Brindley, R. Neu, *Mater. Perform. Charact.* **2019**, *8*, 272.

[11] H. Choe, J. Schneibel, R. Ritchie, *Metall. Mater. Trans. A* **2003**, *34*, 225.

[12] A. Christensen, *Acta Chem. Scand., Ser. A* **1983**, *37*, 519.

[13] A. Misra, J. Petrovic, T. Mitchell, *Scr. Mater* **1998**, *40*, 191.

[14] K. Kishida, Z. Chen, H. Matsunoshita, T. Maruyama, T. Fukuyama, Y. Sasai, H. Inui, M. Heilmaier, *Int. J. Plast.* **2022**, *155*, 103339.

[15] M. Azim, H.-J. Christ, B. Gorr, T. Kowald, O. Lenchuk, K. Albe, M. Heilmaier, *Acta Mater.* **2017**, *132*, 25.

[16] M. Milosavljević, U. Burkhardt, P. Moll, M. König, H. Borrmann, Y. Grin, *Chem. - Eur. J.* **2021**, *27*, 14209.

[17] I. Rosales, J. Schneibel, *Intermetallics* **2000**, *8*, 885.

[18] O. Lenchuk, J. Rohrer, K. Albe, *Scr. Mater.* **2015**, *97*, 1.

[19] S.-P. Sun, S. Gu, Y. Jiang, D.-Q. Yi, *Chin. J. Nonferrous Met.* **2019**, *29*, 115.

[20] O. Lenchuk, J. Rohrer, K. Albe, *J. Mater. Sci.* **2016**, *51*, 1873.

[21] L. Zhu, S. Ida, G. Hasemann, M. Krüger, K. Yoshimi, *Intermetallics* **2021**, *132*, 107131.

[22] Y. Cai, F. Wang, A. Czerny, H.-J. Seifert, B. Nestler, *Acta Mater.* **2023**, *258*, 119178.

[23] T. Soares, Z. Cournia, K. Naidoo, R. Amaro, H. Wahab, K. Merz, *J. Chem. Inf. Model.* **2023**, *63*, 3227.

[24] M. Baskes, *Mater. Sci. Eng., A* **1999**, *261*, 165.

[25] Y. Mishin, *Acta Mater.* **2021**, *214*, 116980.

[26] N. Artrith, A. Urban, G. Ceder, *Phys. Rev. B* **2017**, *96*, 014112.

[27] A. Bartók, M. Payne, R. Kondor, G. Csányi, *Phys. Rev. Lett.* **2010**, *104*, 136403.

[28] R. Drautz, *Phys. Rev. B* **2019**, *99*, 014104.

[29] Y. Zuo, C. Chen, X. Li, Z. Deng, Y. Chen, J. Behler, G. Csányi, A. Shapeev, A. Thompson, M. Wood, S. Ong, *J. Phys. Chem. A* **2020**, *124*, 731.

[30] C. Rosenbrock, K. Gubaev, A. Shapeev, L. Pártay, N. Bernstein, G. Csányi, G. Hart, *npj Comput. Mater.* **2021**, *7*, 1.

[31] G. Sosso, V. Deringer, S. Elliott, G. Csányi, *Mol. Simul.* **2018**, *44*, 866.

[32] A. Bartók, J. Kermode, N. Bernstein, G. Csányi, *Phys. Rev. X* **2018**, *8*, 041048.

[33] Y. Lysogorskiy, C. van der Oord, A. Bochkarev, S. Menon, M. Rinaldi, T. Hammerschmidt, M. Mrovec, A. Thompson, G. Csányi, C. Ortner, R. Drautz, *npj Comput. Mater.* **2021**, *7*, 1.

[34] A. Bochkarev, Y. Lysogorskiy, S. Menon, M. Qamar, M. Mrovec, R. Drautz, *Phys. Rev. Mater.* **2022**, *6*, 013804.

[35] F. Chu, D. Thoma, K. McClellan, P. Peralta, *Mater. Sci. Eng., A* **1999**, *261*, 44.

[36] M. Nakamura, S. Matsumoto, T. Hirano, *J. Mater. Sci.* **1990**, *25*, 3309.

[37] J. Hall, *Phys. Rev.* **1967**, *161*, 756.

[38] S. Zhong, Z. Chen, M. Wang, D. Chen, *Eur. Phys. J. B* **2016**, *89*, 6.

[39] D. Bolef, J. De Klerk, *J. Appl. Phys.* **2004**, *33*, 2311.

[40] O. Thomas, J. Senateur, R. Madar, O. Laborde, E. Rosencher, *Solid State Commun.* **1985**, *55*, 629.

[41] L.-F. Zhu, J. Janssen, S. Ishibashi, F. Körmann, B. Grabowski, J. Neugebauer, *Comput. Mater. Sci* **2021**, *187*, 110065.

[42] S. Menon, Y. Lysogorskiy, J. Rogal, R. Drautz, *Phys. Rev. Mater.* **2021**, *5*, 103801.

[43] X. Yu, Z. Li, P. Jain, H. Gao, S. Kumar, *Acta Mater.* **2021**, *207*, 116654.

[44] A. Gokhale, G. Abbaschian, *J. Phase Equilib.* **1991**, *12*, 493.

[45] H. Okamoto, *J. Phase Equilib. Diffus.* **2011**, *32*, 176.

[46] W. Moffatt, G. E. C. Research, D. Center, *The Handbook of Binary Phase Diagrams*, Number Bd. 4 In Binary Phase Diagrams Handbook, Genium Publishing Corporation, New York **1976**.

[47] R. Kieffer, E. Cerwenka, *Z. Metallkund.* **1952**, *43*, 101.

[48] X. Li, S. Sun, H. Wang, W. Lei, Y. Jiang, D. Yi, *J. Alloys Compd.* **2014**, *605*, 45.

[49] H. Mehrer, H. Schäfer, I. Belova, G. Murch, *Defect Diffus. Forum* **2012**, *322*, 107.

[50] Y. Huang, T. Fu, X. Xu, N. Wang, *J. Phys.: Condens. Matter.* **2021**, *33*, 465402.

[51] S.-H. Ha, K. Yoshimi, K. Maruyama, R. Tu, T. Goto, *Mater. Sci. Eng., A* **2012**, *552*, 179.

[52] I. Gnesin, B. Gnesin, *Int. J. Refract. Met. Hard Mater* **2020**, *88*, 105188.

[53] P. Lejcek, A. Skolakova, *J. Mater. Sci.* **2023**, *58*, 10043.

[54] A. Stukowski, *Modell. Simul. Mater. Sci. Eng.* **2010**, *18*, 025016.

[55] A. Thompson, H. Aktulga, R. Berger, D. Bolintineanu, W. Brown, P. Crozier, P. in 't Veld, A. Kohlmeyer, S. Moore, T. Nguyen, R. Shan, M. Stevens, J. Tranchida, C. Trott, S. Plimpton, *Comp. Phys. Comm.* **2022**, *271*, 108171.

[56] F. Birch, *Phys. Rev.* **1947**, *71*, 809.

[57] F. Murnaghan, *Proc. Natl. Acad. Sci. U.S.A.* **1944**, *30*, 244.

[58] D. Jiang, M. Wu, D. Liu, F. Li, M. Chai, S. Liu, *Metals* **2019**, *9*, 9.

[59] P. Blöchl, *Phys. Rev. B* **1994**, *50*, 17953.

[60] P. Blöchl, C. Först, J. Schimpl, *Bull. Mater. Sci.* **2003**, *26*, 33.

[61] J. Mortensen, L. Hansen, K. Jacobsen, *Phys. Rev. B* **2005**, *71*, 035109.

[62] J. Enkovaara, C. Rostgaard, J. Mortensen, J. Chen, M. Dułak, L. Ferrighi, J. Gavnholt, C. Glinsvad, V. Haikola, H. Hansen, H. Kristoffersen, M. Kuisma, A. Larsen, L. Lehtovaara, M. Ljungberg, O. Lopez-Acevedo, P. Moses, J. Ojanen, T. Olsen, V. Petzold, N. Romero, J. Stausholm-Møller, M. Strange, G. Tritsaris, M. Vanin, M. Walter, B. Hammer, H. Häkkinen, G. Madsen, R. Nieminen, et al., *J. Phys.: Condens. Matter* **2010**, *22*, 253202.

[63] M. Dion, H. Rydberg, E. Schröder, D. Langreth, B. Lundqvist, *Phys. Rev. Lett.* **2004**, *92*, 246401.

[64] Y. Mishin, M. Søorensen, A. Voter, *Philos. Mag. A* **2001**, *81*, 2591.

[65] H. Fujiwara, Y. Ueda, *J. Alloys Compd.* **2007**, *441*, 168.

[66] T. Chart, *High Temp.-High Pressures* **1973**, *5*, 241.

[67] T. Chart, *A Critical Assessment of Thermochemical Data for Transition Metal-Silicon Systems*, Volume 18 Of NPL Report/Chem: NPL Report, National Physical Laboratory, Great Britain **1972**, p. 66+.

[68] I. Tomaszkiewicz, G. Hope, C. Beck, P. O'hare, *J. Chem. Thermodyn.* **1996**, *28*, 29.

[69] I. Tomaszkiewicz, G. Hope, C. Beck, P. O'Hare, *J. Chem. Thermodyn.* **1997**, *29*, 87.

[70] P. O'Hare, *J. Chem. Thermodyn.* **1993**, *25*, 1333.

[71] R. Hultgren, P. Desai, D. Hawkins, M. Gleiser, K. Kelley, *Selected Values of the Thermodynamic Properties of Binary Alloys*, American Society for Metals, Metals Park, OH **1973**, p. 1456.

[72] V. Maslov, A. Neganov, I. Borovinskaya, A. Merzhanov, *Fiz. Goreniya Vzryva* **1978**, *14*, 73.

[73] S. Meschel, O. Kleppa, *J. Alloys Compd.* **1998**, *274*, 193.

[74] Y. Kraftmakher, *Lecture Notes on Equilibrium Point Defects and Thermophysical Properties of Metals*, World Scientific, Singapore **2000**.

[75] H.-E. Schäfer, *Phys. Status Solidi A* **1987**, *102*, 47.

[76] U. Krause, J. Kuska, R. Wedell, *Phys. Status Solidi B* **1989**, *151*, 479.

[77] J. Van Vechten, *Phys. Rev. B* **1986**, *33*, 2674.

[78] L. Elstner, W. Kamprath, *Phys. Status Solidi B* **1967**, *22*, 541.

[79] S. Dannefaer, P. Mascher, D. Kerr, *Phys. Rev. Lett.* **1986**, *56*, 2195.

[80] N. Fukata, A. Kasuya, M. Suezawa, *Jpn. J. Appl. Phys.* **2001**, *40*, 8B L854.

[81] X. Zhang, W. Sprengel, T. Staab, H. Inui, H.-E. Schäfer, *Phys. Rev. Lett.* **2004**, *92*, 155502.

[82] J.P. Perdew, K. Burke, M. Ernzerhof, *Phys. Rev. Lett.* **1996**, *77*, 3865.

[83] J.P. Perdew, K. Burke, M. Ernzerhof, *Phys. Rev. Lett.* **1997**, *78*, 1396.